Response of atmospheric quasi-stationary waves to La Niña conditions in Northern Hemisphere winter

Received: 20 August 2021 | Revised: 21 January 2022 | Accepted: 23 February 2022

DOI: 10.1002/qj.4261

Quarterly Journal of the Royal Meteorological Society RMetS

RESEARCH ARTICLE

Response of atmospheric quasi-stationary waves to La Niña conditions in Northern Hemisphere winter

G. Wolf[1,2] | **D.J. Brayshaw**[1,2] | **N.P. Klingaman**[1,2]

[1]Meteorology Department, University of Reading, Reading, UK

[2]National Center for Atmospheric Sciences, University of Reading, Reading, UK

Correspondence
G.A. Wolf, Meteorology Department, University of Reading, PO Box 243, Reading RG6 6BB, UK
Email: g.a.wolf@reading.ac.uk

Funding information
UK Natural Environment Research Council (NERC) for the ODYSEA project NERC Independent Research Fellowship, Grant/Award Numbers: NE/M006085/1, NE/L010976/1

Abstract

Large-scale atmospheric quasi-stationary waves (QSWs) are strongly linked to synoptic variability and extreme events such as blocking and heatwaves. It is therefore essential to gain a deeper insight into the drivers of QSW variability. Previous research highlighted the El Niño Southern Oscillation as one of the main drivers for global QSW variability with La Niña conditions of particular interest because of their link to anomalous strong QSW amplitudes. This connection between La Niña and QSW activity in the Northern Hemisphere is analysed in this study using a set of aquaplanet experiments with a slab ocean, mimicking La Niña conditions of varying strengths. The experiments demonstrate La Niña conditions are consistent with a weaker zonal mean Hadley cell and a corresponding northward shift in the midlatitude wave guide associated with strong meridional gradients in absolute vorticity. The QSW region generally follows this shift in the wave guide with an overall increase in QSW amplitudes along a slightly weaker mean vorticity gradient. For weak to moderate modifications of the ocean heat flux convergence, there is an approximately linear relationship with the associated QSW response, though for stronger slab heat fluxes the overall response becomes highly nonlinear. It is therefore concluded that the ENSO state may have significant consequences for QSW activity across the Northern Hemisphere.

KEYWORDS

aquaplanet, El Niño Southern Oscillation, quasi-stationary wave

1 | INTRODUCTION

Weather conditions in the midlatitudes are often thought to be dominated by the effects of synoptic-scale features, typically evolving on time-scales from hours to a few days. Recently, however, there has been considerable interest in more persistent weather regimes, for example, blocking anticyclones or "blocks", which preferentially occur at the exit of the midlatitude jet (Masato *et al.*, 2014). Such blocks are often part of a longitudinally extended, slowly evolving "quasi-stationary" wave (QSW; e.g., Nakamura *et al.*, 1997) with lifetimes of several days or weeks.

These QSWs are important, because they are frequently associated with strong variations in surface climate and extreme weather events (Screen and Simmonds, 2014; Wolf *et al.*, 2018b), potentially across a wide range of locations through so-called teleconnections (Branstator, 2002; Ding and Wang, 2005). The midlatitude jet plays a key role in these teleconnections, potentially acting to trap Rossby wave energy through acting as a wave guide (Hoskins and Ambrizzi, 1993; Manola *et al.*, 2013), which means the jet stream has ability to trap Rossby wave energy. Previous research has established that anomalous QSW activity can be strongly associated with some large-scale climate patterns (Wolf *et al.*, 2018b), and provides an alternative dynamical perspective (compared to, e.g., classical pattern correlations) on how large-scale climate indicators impact on regional weather events. One such large-scale climate pattern is the El Niño–Southern Oscillation (ENSO) phenomenon, which causes strong changes in the general circulation of the atmosphere and its teleconnections (Yeh *et al.*, 2018). It is therefore important to understand the processes through which ENSO impacts on regional weather behaviours through its modification of the overall atmospheric circulation.

After the onset of ENSO, a stationary and large-scale wave response, resembling the Pacific–North America pattern, can typically be observed in the following winter (Shabbar *et al.*, 1997). Besides this long-wave response, Chen (2002) further identified shorter wavetrains with a wavenumber range of 4–15 during strong negative ENSO phases, which they associated with cold surge vortices in the Philippine Sea. These cold surges can further be associated with a stronger Asian jet and a zonally localised intensified Hadley cell (Yen and Chen, 2002) and are closely linked to the ENSO phase, with more cold surges during La Niña (Zhang *et al.*, 2011).

This paper focuses on the physical process of this connection between La Niña and QSW activity in the Northern Hemisphere midlatitudes, seeking to understand the underlying mechanisms by using reanalysis and bespoke aquaplanet experiments (APEs) emulating observed ENSO conditions. The latter provides a framework for investigating the behaviour of the global circulation in "full" GCMs but with simplified boundary conditions (e.g., Brayshaw *et al.*, 2008; Saulière *et al.*, 2012; Blackburn and Hoskins, 2013; Merlis and Held, 2019). The impact of changes in tropical SST gradients and zonal SST anomalies in particular were investigated in detail in Gastineau *et al.* (2011) using an APE set-up: a weakening of the meridional SST gradient or inclusion of zonally asymmetric SSTs leads to a weakening and broadening of the Hadley cell, along with associated changes in the structure of the midlatitude jet. The decision to focus specifically on La Niña conditions is due to the fact that this phase of ENSO is associated with increased QSW amplitudes, whereas El Niño conditions are rather associated with the absence of strong QSW amplitudes (Wolf *et al.*, 2020). Further motivation for this focus can be given by the findings that in general strong QSW amplitudes can be associated with extreme events or strong anomalous weather conditions (Wolf *et al.*, 2018b).

The remainder of this paper is organized as follows. Section 2 presents the data, the set-up of the aquaplanet experiments and the method to calculate the QSWs. Section 3 presents the anomalous QSW patterns during El Niño and La Niña phase in ERA-Interim to provide a benchmark evaluation of the APE simulations. In Section 4 the mechanisms through which ENSO influences midlatitude QSWs are discussed. The key conclusions of this paper are summarized in Section 5.

2 | METHOD

2.1 | Observational datasets

The primary observational datasets used in this study are derived from the ERA-Interim (Dee *et al.*, 2011) reanalysis on a grid with $0.75° \times 0.75°$ resolution. For ENSO, the monthly Niño 3.4 index is used to characterize the strength of the phase of the ENSO, downloaded from the website of the National Oceanic and Atmospheric Administration (http://www.cpc.ncep.noaa.gov; accessed 11 March 2022).

2.2 | QSW identification

To identify QSWs the method of Wolf *et al.* (2018b) is used. The amplitude of the QSW is a phase-independent non-negative measure of the waviness of the anomalous meridional wind v', which is defined as $v' = \widetilde{v} - \bar{\widetilde{v}}$ with $\widetilde{v}$ being the 15-day low-pass filtered meridional wind to remove the faster transients and $\bar{\widetilde{v}}$ the 15-day low-pass filtered daily based climatology of the meridional wind to remove the climatological background signal. A Hilbert transform (as in Zimin *et al.*, 2003) is then applied to v' at each latitude circle, keeping only a predefined wavenumber range (about 4 to 8 in midlatitudes). Instead of using a fixed wavenumber range, we here use a meridionally varying wavenumber range, following the maximum of the zonal mean power spectra of v' (details in Wolf *et al.*, 2018b).

An instructive illustration of the method can be seen in Figure 1 of Wolf *et al.* (2018b). The definitions of v' allows the identification of slowly moving, large-scale waves. The Hilbert transform converts this wind quantity, which is represented by positive and negative values, into a strictly

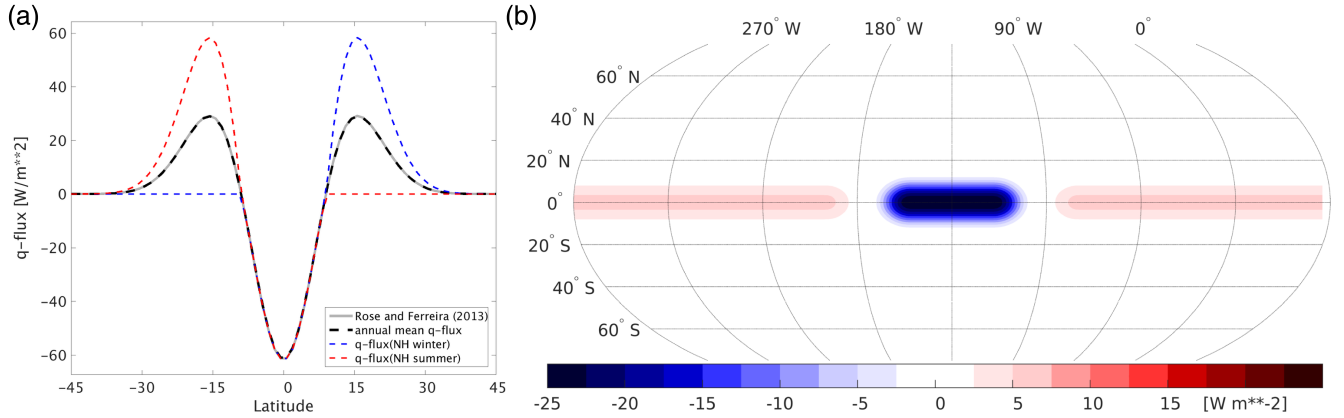

FIGURE 1 q-flux profile and anomaly for the auqaplanet experiments. (a) shows zonally averaged q-flux for all aquaplanet experiments. Thick grey line shows the profile taken from Rose and Ferreira (2013) with $N = 20$. Blue and red lines show the q-flux for NH winter and summer seasons. Thick dashed black line shows the annual mean q-flux profile. (b) shows the 2D pattern for the q-flux anomaly of $-25\,\mathrm{W/m^2}$ [Colour figure can be viewed at wileyonlinelibrary.com]

positive field, the so-called envelope field. This envelope field measures the waviness of v' and therefore allows the identification of wave packets. In order to analyze the occurence of waves in composites or climatologies, the envelope field has an important advantage compared to v'. As v' consists of positive and negative values, composites can be hard to interpret, because positive and negative values can cancel out in the case of waves not occuring at the exact same location. However, the composite of the envelope field will measure the average wave strength of the composited waves, independent of their phasing. When we mention wave amplitudes in the following, we always refer to this averaged envelope field. If we refer to anomalous wave amplitudes, this is the anomalous envelope field relative to climatology and therefore can be represented by both positive and negative values.

2.3 | Aquaplanet control run (CTRL)

To understand the atmospheric response to ENSO, a series of APEs are conducted (e.g., Blackburn and Hoskins, 2013) using a full atmospheric GCM coupled to a "slab" ocean. In contrast to many APEs (which use prescribed sea surface temperatures, SSTs), the slab ocean allows the prescription of a spatial pattern of heat-flux convergence (the so-called "q-flux") to account for a redistribution of heat by the ocean in an energetically consistent manner (Voigt *et al.*, 2016). We use a modified configuration of the Global Ocean Mixed Layer 2.0 coupled configuration of the Met Office climate model (MetUM-GOML; Hirons *et al.*, 2015; Peatman and Klingaman, 2018). MetUM-GOML comprises many columns of a one-dimensional ocean model, based on the K Profile Parametrization (KPP) of Large *et al.* (1994), coupled to the Global Atmosphere 6.0 configuration of the Met Office atmospheric general circulation model (Walters *et al.*, 2017). Here, we configure KPP as a single-layer slab of 30 m depth, with no vertical mixing or diffusion. The atmosphere and ocean share a horizontal resolution of 1.875° longitude × 1.25° latitude, on a regular grid, which is approximately 200 km in longitude (at the Equator) × 150 km in latitude. The atmospheric model has 85 points in the vertical and a model lid at 85 km.

The purpose of this investigation is to understand the extratropical atmospheric QSW response to ENSO and, in particular, to La Niña-like events. As a starting point, it is therefore not only necessary to achieve a "reasonable" representation of the zonal-mean circulation (particularly the Hadley Cell and midlatitude jets to ensure, e.g., appropriate stationary Rossby Wave propagation characteristics), but it must also be acknowledged that ENSO events (i.e., both La Niña and El Niño) take place against a background which is itself zonally asymmetric (i.e., an east–west dipole of SST is clearly visible in the tropical Pacific under ENSO-neutral conditions). As such, in contrast to most APEs, we therefore choose to define an asymmetric set of forcings for the control run (CTRL), with enhancements to this asymmetry being broadly interpreted as "La Niña-like" and weakening being interpreted as "El Niño-like".

The control run (CTRL) forcing can therefore be described in two parts. Firstly, a zonal-mean oceanic meridional heat transport (OHT) in the aquaplanet experiments is prescribed based upon a zonally symmetric q-flux (convergence of ocean heat transport) profile, using equation (1) in Rose and Ferreira (2013)

$$OHT = \psi \sin(\phi)\ \cos(\phi)^{2N} = \psi\ x\ (1 - x^2)^N, \qquad (1)$$

where $\psi = \sqrt{1+2N}\,\{(1+2N)/(2N)\}^{N}\,1.5\times10^{15}$ W, $x = \sin(\phi)$, ϕ is latitude, and $N = 20$ (thick grey line in Figure 1a): effectively, this is associated with a meridional OHT away from the Equator into the subtropics in the annual-mean (black line in Figure 1a). Note that the q-flux is energetically balanced, that is, there is no net addition in the global (spatial) average. To avoid unrealistic patterns of heating/cooling that can occur in experiments lacking a seasonal cycle (e.g., runaway cooling at the winter pole), a seasonal cycle is included for both the incoming solar radiation at the top of the atmosphere and in the ocean's q-flux profile. For the ocean q-flux, this is achieved by associating all the subtropical heat flux convergence into the summer hemisphere (i.e., the subtropical q-flux is strongly positive in the winter hemisphere and zero in the summer hemisphere as indicated by the red and blue dashed lines in Figure 1a), while the equatorial divergence is unchanged. Winter is taken as being December–April in the Northern Hemisphere and June–October in the Southern Hemisphere, with a linear transition between the two states in May and November. The resulting seasonally varying q-flux distributions therefore match the original distribution in the annual-mean while qualitatively resembling the observed cycle of tropical OHT recorded in Fasullo and Trenberth (2008, figure 7c therein).

Secondly, a zonally asymmetric q-flux anomaly at the Equator is added to mimic the real-world zonal asymmetry of the East Pacific SST cold tongue. This is done by a $-25\,\mathrm{W/m^{-2}}$ q-flux anomaly between 155°W and 115°W (with a cosine squared decay for the adjacent 20° longitude and 15° latitude) which is balanced by a constant, positive q-flux, added to all other longitudes (with a similar cosine-squared meridional tapering). This is shown in Figure 1b.

As the lower boundary forcing of the Northern and Southern Hemispheres is symmetric (subject to matching the phase of the seasonal cycle), the output data for the two hemispheres is concatenated (the statistics of the extratropical QSWs in each hemisphere are assumed independent). This leads to a total simulation time of 100 years for one hemisphere after a spin-up time of nine years in each experiment (including the control run).

The resulting CTRL experiment produces a reasonable representation of the zonally asymmetric surface temperatures seen in the equatorial Pacific (in terms of spatial extent and magnitude). Overall, as shown in Figure 2, CTRL reproduces a reasonably realistic atmosphere with a comparable meridional surface temperature gradient to ERA-Interim in midlatitudes (Figure 2a), though it is typically somewhat warmer than that observed in ERA-Interim. The resulting seasonal-mean zonal winds at 300 hPa are qualitatively similar to those observed in the wintertime Northern Hemisphere (Figure 2b), peaking in strength at around 32° latitude and $42\,\mathrm{m\,s^{-1}}$ with little seasonal variation. The seemingly inconsistency of a smaller temperature gradient but stronger jet of the model is consistent with the more complex real-world situation where a weakening of the jet over land and the strong northward tilt over the Atlantic occurs (Brayshaw *et al.*, 2009; Saulière *et al.*, 2012). Such effects result in a weaker and broader jet from a zonal average perspective. Consistent with this overall similarity in jet structure, the power

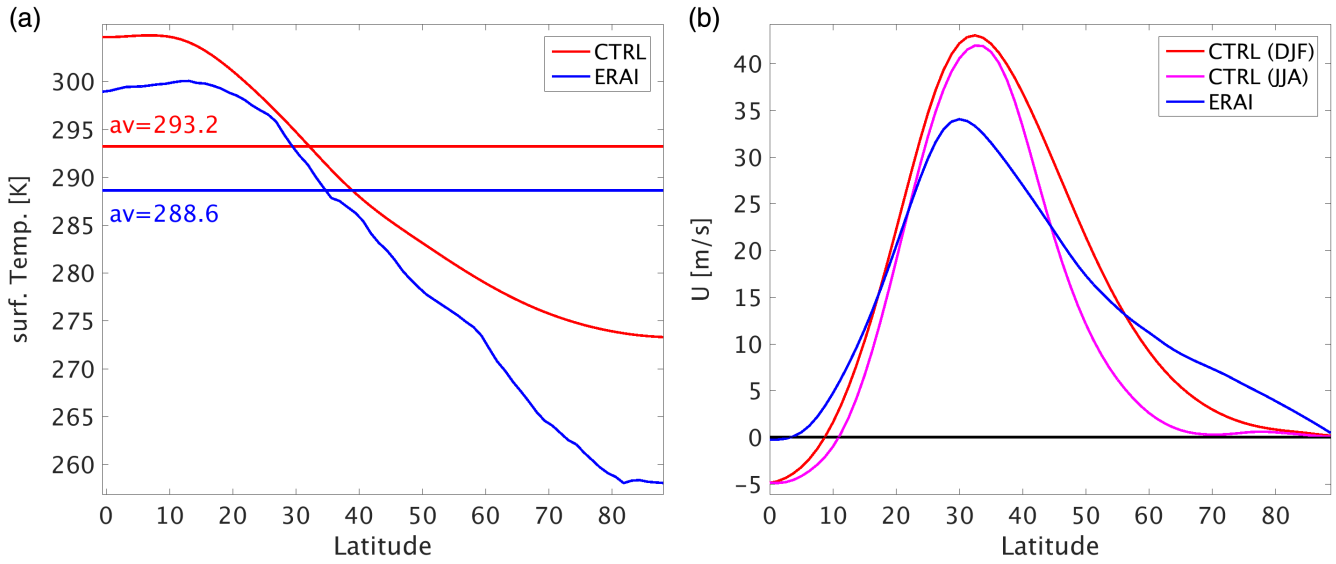

FIGURE 2 Surface temperatures and jet strengths for CTRL and ERA-Interim. (a) shows zonally averaged annual mean surface temperature for CTRL and ERA-Interim on the Northern Hemisphere. (b) shows zonally averaged zonal wind at 300 hPa for CTRL in DJF and JJA and for ERA-Interim in DJF [Colour figure can be viewed at wileyonlinelibrary.com]

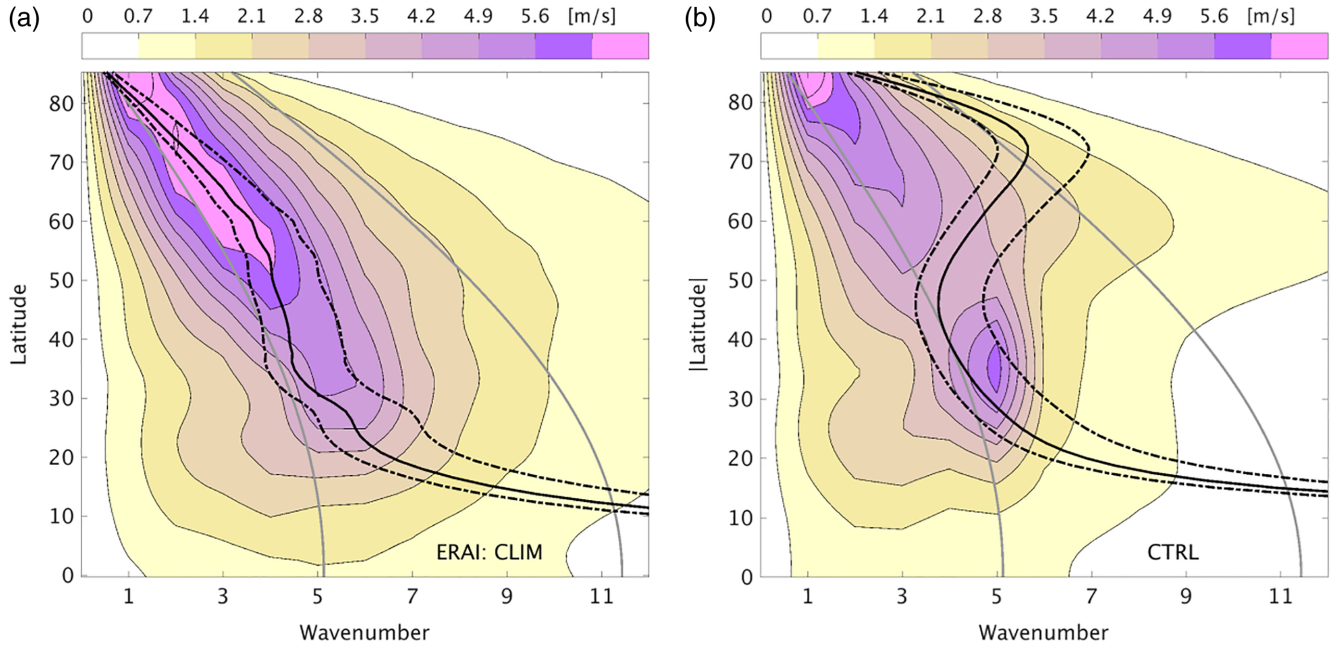

FIGURE 3 Power spectra of time-filtered meridional wind v' at 300 hPa for (a) ERA-Interim and (b) CTRL. The applied time filter is the same as for the calculation of QSW amplitudes (Subsection 2.2). Grey contour lines show the chosen wavenumber range at each latitude, used to calculate the QSWs. Black lines show the estimated wavenumber, derived from the barotropic Rossby wave dispersion relation for three different phase speeds: 0.1 times the mean zonal wind (solid line), 0 and 0.5 times the mean zonal wind (dashed lines) [Colour figure can be viewed at wileyonlinelibrary.com]

spectra of v' (the time-filtered meridional wind anomalies used to identify QSW; subsection 2.2) for CTRL resembles that of observations, with a midlatitude peak around the jet core (35° latitude) near zonal wavenumber 5 (Figure 3).

Overall, this suggests that the QSW behaviour (which are calculated at 300 hPa) and SST (to q-flux anomalies) are likely to be broadly comparable to observed Earth-like conditions for Northern Hemisphere winter irrespective of the phase of the seasonal cycle within the APE simulation (consistent with the large surface thermal inertia of the APE slab-ocean compared to "real world" experiments with land, suppressing the seasonal cycle of surface temperature). As the Northern Hemisphere winter response to ENSO is the central focus of this paper, we therefore choose to maximize the available data and therefore compare the annual-mean behaviour of the APEs with DJF in ERA-Interim (i.e., using the full 100 years of model simulation rather than discarding non-winter months).

2.4 | Aquaplanet experiments

Having established the framework for the control run, La Niña conditions are emulated in a series of APEs by re-scaling the zonally asymmetric part of the control run forcing (i.e., the pattern shown in Figure 1b is amplified). Three experiments are produced (Table 1) by adding steps of $-25\,\mathrm{W/m^{-2}}$ to the q-flux anomaly to obtain a chain of increasing La Niña strengths: weak (EXP025), moderate (EXP050) and strong (EXP075) La Niña conditions.

To provide context and to ensure that the magnitude of the forcing is appropriate, the associated minimum temperature anomalies for the APEs, averaged for the whole climatology, are given in the third column of Table 1. For comparison, the eight strongest observed La Niña seasons in DJF (using the Niño 3.4 index) have a minimum mean temperature anomaly of −1.8 K (average for the whole time period), or −3.3 K for the mean minimum monthly temperature. This therefore suggests that the APEs provide a representation of La Niña-like conditions in the tropical Pacific comparable to those observed in the real world in terms of approximate spatial scale and magnitude.

The advantage of the simpler aquaplanet set-up, compared to more realistic GCMs, is that it provides a simple framework to analyze and understand the basic connection between La Niña and the QSW response. It is also of advantage to understand the degree of possible simplifications without losing the capability to reproduce the qualitatively same QSW response as for the real-world phenomena. The results of the simplified aquaplanet model will then also help in the interpretation of more realistic models that usually come along with more difficult interpretations.

TABLE 1 Aquaplanet experiments

Experiment	Name	q-flux anomaly ($W\,m^{-2}$)	$\min(T_{surf} - T_{(surf,CTRL)})$ (K)
CTRL	Control run	−25	0.0
EXP025	Weak La Niña	−50	−0.7
EXP050	Moderate La Niña	−75	−2.0
EXP075	Strong La Niña	−100	−3.8

Note: The first two columns show the abbreviations and a short description of the experiments used in the text. The third column specifies the negative q-flux anomaly (Figure 1b). The fourth column gives the associated surface temperature anomalies, compared to the control run.

3 | QSW DURING LA NIÑA IN REANALYSIS AND APES

To evaluate the ability of the APEs to reproduce the QSW response to La Niña, the anomalous spatial patterns of QSW activity and the meridional wind's power spectra are each contrasted with observations.

The observed spatial pattern anomalies in QSWs during El Niño and La Niña in DJF are shown in Figure 4 (compositing the eight seasons with the strongest positive and negative mean values of the Niño 3.4 index). Consistent with previous studies (Wolf *et al.*, 2020), during La Niña the QSW anomaly pattern strengthens over the Pacific and parts of North America, with increased values further east along a band at lower latitudes. Over the North Atlantic and Europe north of 50°N, one can identify slightly decreased values. A broadly opposing pattern can be observed in El Niño (suggesting the QSW response is somewhat linear to ENSO state), though there are qualitative differences (e.g., the eastward extension of the QSW anomaly signal over North America occurs at lower latitude in La Niña than in El Niño). Figure 4c, d also show this opposing pattern for the zonal averages of QSW amplitudes between 225°W and 45°W for the eight strongest ENSO seasons (as shown in Figure 4a, b), but also for the five and 18 strongest seasons with their temporal variability (error bars). This comparison shows the general and consistent difference in QSW response to El Niño and La Niña. The five most extreme La Niña events even indicate a circumglobal coherent band of increased QSW amplitudes (not shown here), associated with the peak of zonally averaged QSW amplitudes at 40°N also exceeding the higher-latitude peak (Figure 4d).

Results of the APEs for La Niña conditions show qualitative similarities to the observed La Niña response: at higher latitudes, extra-tropical QSW anomalies are increased upstream (around 225°W) and decreased downstream (around 90°W), with increased QSW anomalies at midlatitudes at 30–50°N (Figure 5a). This pattern is qualitatively consistent across each of the APE experiments (EXP025, 050 and 075; not shown), with stronger forcing leading to more strongly positive midlatitude QSW anomalies and negative high-latitude QSW anomalies (zonal averages for all three APEs in Figure 5b).

However, there are several areas where the APE patterns diverge from the observed La Niña response. In contrast to the reanalysis QSW pattern (Figure 4b), the lower-latitude increased QSW anomalies in the APE clearly span all longitudes along the subtropical jet in an almost zonal band rather than being strongly focussed in the Atlantic/Pacific region (Figure 5a), consistent with the absence of strong zonal forcing asymmetries (such as land and orography) in the APE framework. The negative QSW anomalies in high latitudes (poleward of 60°) must also be interpreted with some caution given the lack of sea ice and consequent strong high-latitude surface temperature gradients in the APE framework.

Further insight into the QSW response can be gained through the power spectra of the anomalous meridional wind, v', used to identify QSWs (Figure 6, also subsection 2.2). In observations, the eight strongest La Niña seasons are associated with increased values in the power spectra for zonal wavenumbers about 4 to 6 in midlatitudes (30°–50°N; Figure 6a), broadly corresponding to an increase in the strength of the most dominant wavenumbers in this region (around wavenumber 5 at 35–40 °N, Figure 3a). Similarly, EXP075 shows increased values of v' in the midlatitudes with a strong peak at wavenumber 5 around 40°N (Figure 3b). Similar positive peaks at 40°N are also visible for EXP025 and EXP050, although with weaker values and occurring at wavenumber 4.

The modelled APE QSW response to the idealised La Niña-like forcing in EXP025-075 is therefore qualitatively consistent with the observed La Niña response in ERA-Interim, both in spatial pattern and meridional wind power spectra (for all three experiments), and increasingly asymmetric tropical q-flux forcing (i.e., moving from EXP025 to EXP075) leads to increasingly strong midlatitude QSWs.

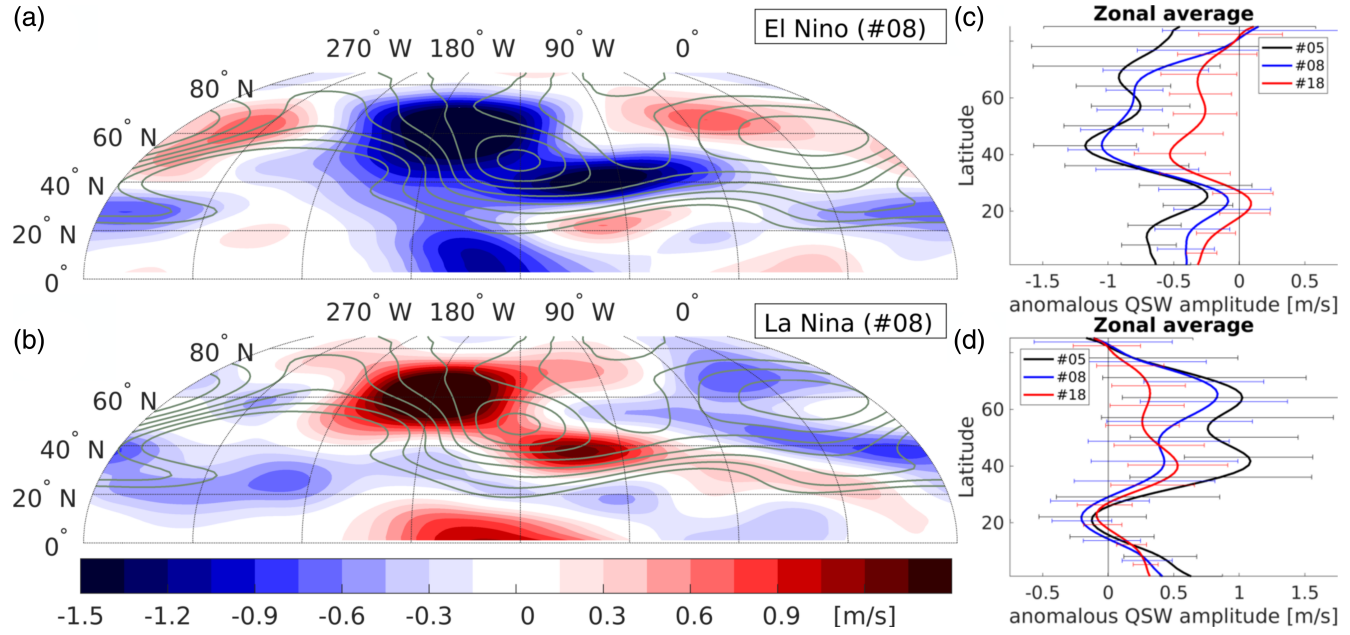

FIGURE 4 Anomalous QSW amplitudes at 300 hPa for ERA-Interim in DJF during La Niña and El Niño. Shading shows anomalous QSW amplitudes, in (a) for the eight strongest El Niño seasons, in (b) for the eight strongest La Niña seasons. The strength of the La Niña/El Niño season is defined by the seasonal average of the Niño 3.4 index. Grey contour lines show DJF QSW climatology, spaced every 0.75 m s^{-1} starting with 7.5 m s^{-1}. (c) and (d) show the zonal averages between 225°W and 45°W for (a) and (b) using the eight strongest El Niño and La Niña years (label #08), as well as for the five strongest (label #5) and 18 strongest (label #18) years. Errorbars show the standard error of the mean (standard deviation of the annual means, divided by the square root of the numbers of years, reduced by one) [Colour figure can be viewed at wileyonlinelibrary.com]

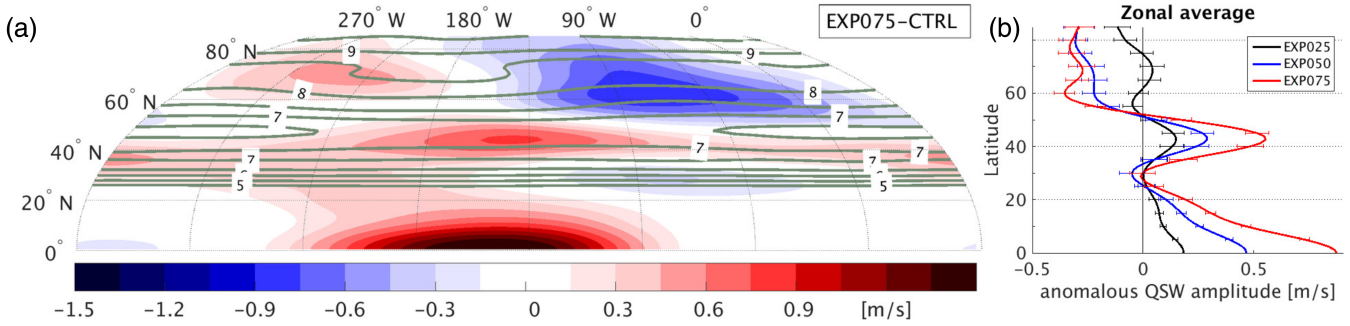

FIGURE 5 Anomalous QSW amplitudes at 300 hPa for strong La Niña phase. Shading in (a) shows anomalous QSW amplitudes (EXP075-CTRL). Grey contour lines show QSW climatology, spaced every 0.5 m s^{-1} starting with 4 m s^{-1}. (b) shows the zonal average of the anomalous QSW amplitudes between 225°W and 45°W. Errorbars show the standard error of the mean (standard deviation of the annual means, divided by the square root of the numbers of years, reduced by one) [Colour figure can be viewed at wileyonlinelibrary.com]

4 | MECHANISMS FOR QSW ANOMALIES

Having established that the APE experiments qualitatively capture the general behaviour of the QSW response to La Niña-like forcing, the physical process through which this response occurs is proposed. The Strong La Niña experiment (EXP075) is used throughout the following discussion to illustrate the process, but consistent (though weaker) responses can be seen in both EXP025 and EXP050 when compared to the control run CTRL.

The zonal-mean response of the tropospheric meridional circulation (i.e., EXP075-CTRL) is shown in Figure 7. The enhancement of the zonal asymmetry in the La Niña-like forcing leads to a clear weakening and broadening of the Hadley cell, a poleward shift in the upper tropospheric jet (Figure 8d) and poleward shift of the Ferrel cell, consistent with previous studies (e.g., Gastineau *et al.*, 2011).

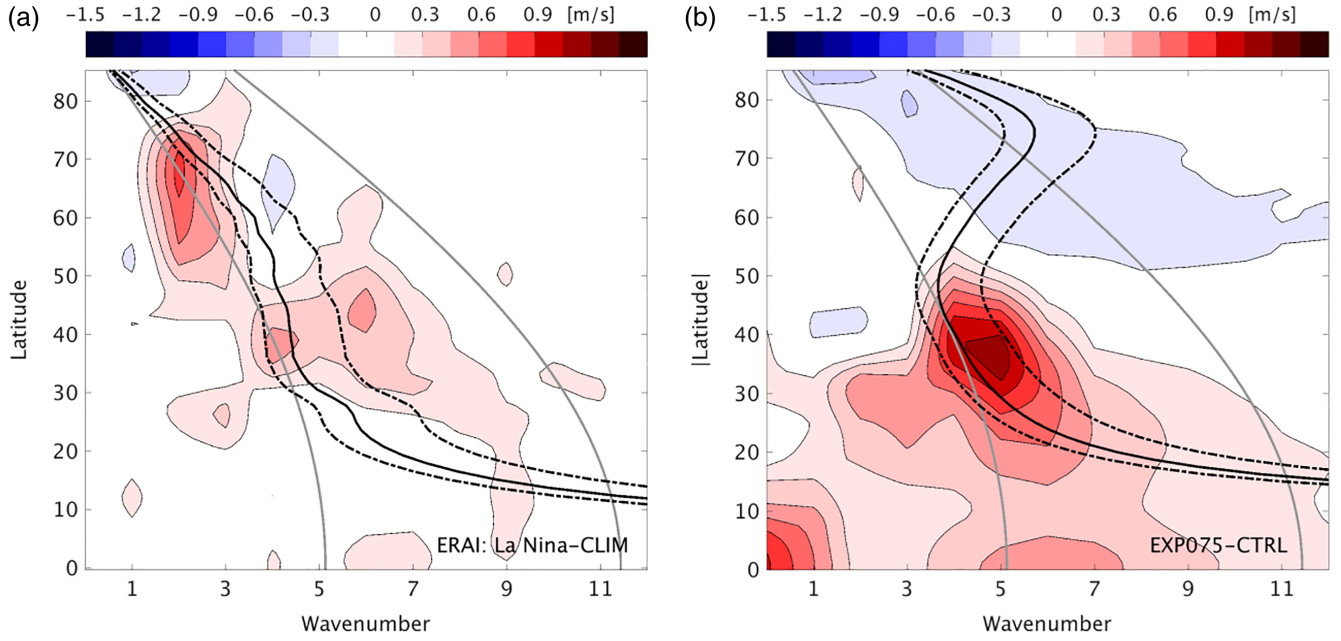

FIGURE 6 Anomalous power spectra of time-filtered meridional wind v' at 300 hPa during strong La Niña phase. The applied time filter is the same as for the calculation of QSW amplitudes (Subsection 2.2). Anomalies are calculated as the deviation from climatology for (a) ERA-Interim and (b) the control run for EXP075, as shown in Figure 3. Grey contour lines show the chosen wavenumber range at each latitude, used to calculate the QSWs. Black lines show the estimated wavenumber, derived from the barotropic Rossby wave dispersion relation for three different phase speeds: 0.1 times the mean zonal wind (solid line), 0 and 0.5 times the mean zonal wind (dashed lines) [Colour figure can be viewed at wileyonlinelibrary.com]

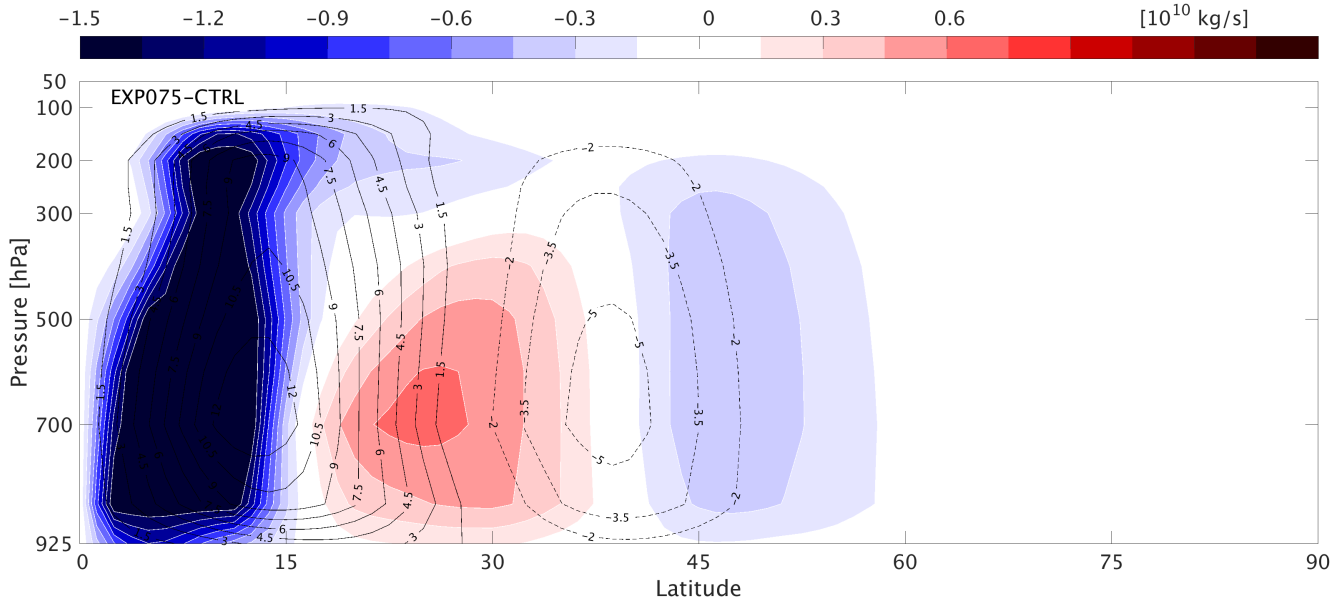

FIGURE 7 Meridional streamfunction. Solid (dashed) contours show positive (negative) values for the meridional streamfunction of CTRL. Shading shows the deviation of the meridional streamfunction of EXP075 from CTRL [Colour figure can be viewed at wileyonlinelibrary.com]

The meridional extension of the Hadley cell is consistent with a northward shift of the jet on the poleward side of the q-flux anomaly (Figure 8b), in agreement with Saulière *et al.* (2012). This poleward shift is again consistent between the different APEs, with an increased poleward shift for increased q-flux anomaly strength (Figure 8c). ERA-Interim shows a very similar northward shift of the jet during La Niña (Figure 8a).

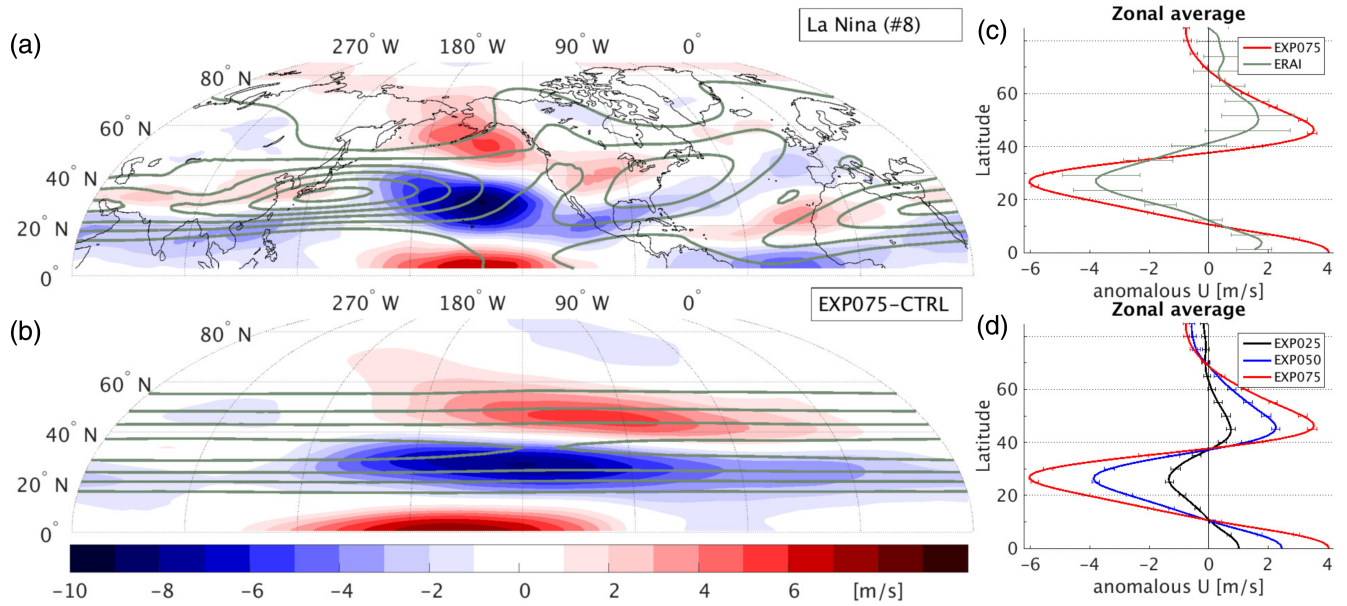

FIGURE 8 Eastward wind at 300 hPa. (a, c) show results for ERA-Interim (eight strongest La Niña seasons), (b, d) for the APE EXP075. Shading in (a, b) shows anomalous eastward wind as deviation (a) from climatology and (b) from the control run CTRL. Contours show climatological values for ERA-Interim in (a) and the control run CTRL in (b), spaced every 10 m s^{-1}, excluding the 0 m s^{-1} contour (only positive contours visible). Zonal averages (c, d) are calculated between 225°W and 45°W. Errorbars show the standard error of the mean (standard deviation of the annual means, divided by the square root of the numbers of years, reduced by one) [Colour figure can be viewed at wileyonlinelibrary.com]

However, locally there are regions where the Hadley cell strengthens with stronger ascent in the Tropics in the far upstream region of the *q*-flux anomaly (not shown).

A poleward shift can also be seen in the meridional vorticity gradient for both ERA-Interim (Figure 9a) and EXP075 (Figure 9b). The anomalies in EXP075 lead to overall weaker total gradients; this can be concluded from the negative anomalous values, lying in the band of peak intensity for the meridional gradient of CTRL at 30°N. Further, both ERA-Interim and EXP075 seem to indicate a slight upstream intensification of the gradient (between 315° and 225°W).

Barotropic Rossby wave theory suggests that waveguides are typically associated with regions of strong medidional gradients of absolute vorticity (e.g., Hoskins and Ambrizzi, 1993). Figure 10 shows the anomalous QSW amplitudes (from Figure 5a) versus the meridional gradient of absolute vorticity (Figure 9b) for all gridpoints between 20 and 50°N. This comparison clearly shows that the strength of the meridional vorticity gradient is directly related to the QSW anomaly magnitude in the region immediately upstream (225° to 135°W) and downstream (135° to 0°W) of the *q*-flux anomaly, suggesting waveguide-like behaviour is occurring. The upstream (green dots) and downstream (red dots) regions show a strong and approximately linear relationship between anomalous QSW amplitudes and anomalies in the meridional vorticity gradient, indicating that the QSW anomalies are following the shift of the waveguide, but with overall slightly increased QSW anomalies (all points shifted towards higher QSW anomalies). The remote region (blue points) represents a slightly different scatter pattern. One can identify overall slightly increased QSW anomalies (mean value given by thick blue and white encircled point), but weaker anomalies in the meridional vorticity gradient (smaller spread along the *x*-axis). This can be explained by the different waveguide anomalies of the different regions. The far upstream waveguide is slightly stronger and tighter (Figure 9b), but does not have the poleward shift that can be seen in the other regions, which is responsible for the stronger anomalies in the meridional vorticity gradient. It is therefore diffficult to assess the potential role (or otherwise) of circumglobal propagation of QSW actvitiy (and hence resonance effects proposed by, for example, Petoukhov *et al.*, 2013).

5 | SUMMARY AND DISCUSSION

In previous studies we have shown a strong link between QSWs and synoptic variability and extreme events over Europe (Wolf *et al.*, 2018b). We also identified patterns of sea surface anomalies (SST and sea ice) which are strongly associated with QSW patterns (Wolf *et al.*, 2020). The most

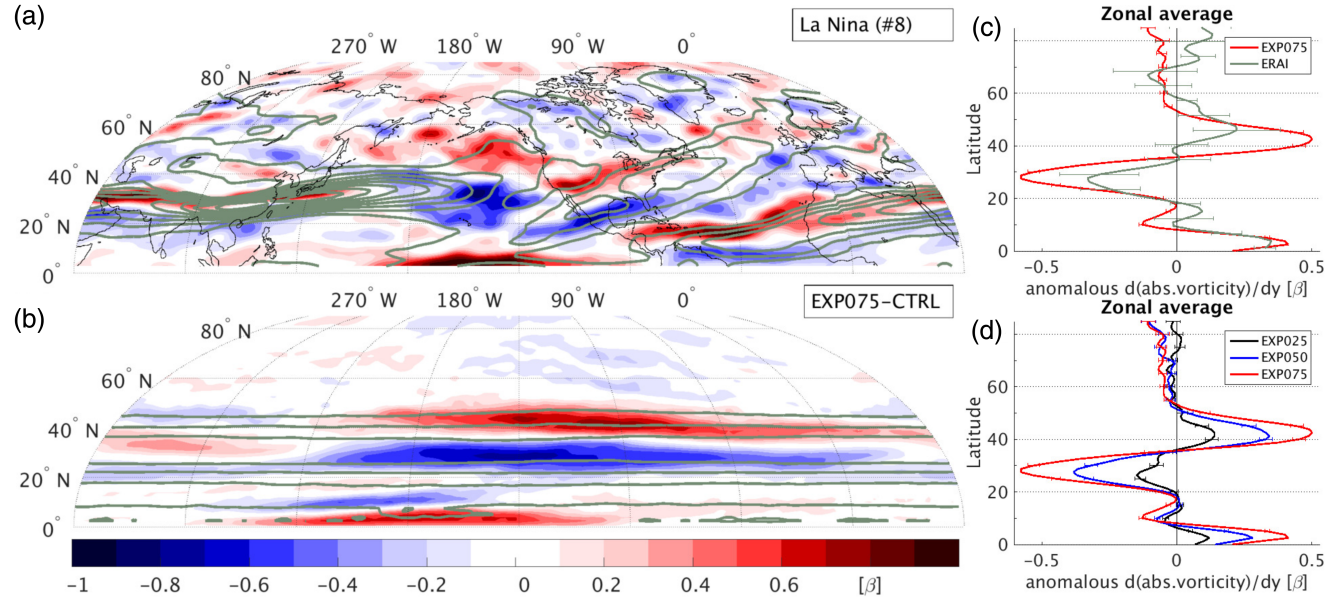

FIGURE 9 Meridional gradient of absolute vorticity at 300 hPa. (a, c) show results for ERA-Interim (eight strongest La Niña seasons), and (b, d) for the APE EXP075. Colour shading in (a, b) shows anomalous meridional gradient of absolute vorticity as deviation from climatology in (a) and from the control run CTRL in (b). Values are normalized by β. Grey contours show climatological values for ERA-Interim in (a) and the control run CTRL in (b), spaced every 0.75 β starting with 0.75 β. Zonal averages (c, d) are calculated between 225°W and 45°W. Errorbars show the standard error of the mean (standard deviation of the annual means, divided by the square root of the numbers of years, reduced by one) [Colour figure can be viewed at wileyonlinelibrary.com]

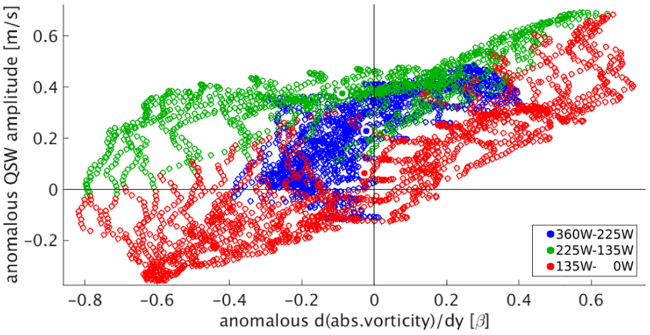

FIGURE 10 Scatter plot between anomalous meridional gradient of absolute vorticity and wave amplitude (both at 300 hPa) for the experiment EXP075-CTRL. Anomalies are taken from Figures 5 and 9b for latitudes between 20 and 50°N. Mean values for all grid points are given by the thick points with surrounding white circles. Different colours indicate different longitudinal regions (given in the legend) [Colour figure can be viewed at wileyonlinelibrary.com]

dominant connection occurs during strong positive and negative phases of ENSO. This present study investigates the mechanism for this behaviour using aquaplanet experiments (APEs).

During the La Niña phases, positive QSW amplitude anomalies can be observed in the Pacific and parts of North America from low towards high latitudes, which further extends downstream along lower latitudes, whereas negative QSW amplitude anomalies occur in the North Atlantic and Europe north of 50°N. This anomalous wave pattern is reproduced by a set of APEs with negative tropical q-flux anomalies to emulate La Niña conditions. Increasing values of the negative q-flux anomalies lead to a strengthening of the anomalous QSW pattern. Consistent with the relatively uniform global boundary conditions applied in the aquaplanet experimental configuration, but in contrast to the reanalysis data, the APEs show positive QSW amplitude anomalies for all longitudes along the subtropical jet at low latitudes.

Under La Niña conditions, the general circulation shows a weaker zonal mean Hadley cell, which expands further north and which is associated with a northward shift of the strong midlatitude meridional vorticity gradient. This northward shift mainly occurs in the direct upstream and downstream region of the negative q-flux anomaly, whereas further upstream an increase of the gradient without any northward shift can be observed. In this far upstream region, one can observe a locally intensified Hadley cell, all in agreement with the findings of Chen (2002). Linking the anomalous QSW amplitudes to the changes in the meridional vorticity gradient shows that the QSW anomalies mainly follow the shift of the vorticity gradient, supporting its importance as a waveguide for these QSWs. But further to the linear relationship between meridional vorticity gradient and QSW amplitude, one can overall observe an increase of QSW amplitudes along

the subtropical jet with a slightly weaker mean vorticity gradient.

Most of the results suggest an approximately linear relationship between the strength of La Niña, given by the q-flux anomaly, and the strength of the anomalous response patterns (SST anomalies, QSW, zonal wind, meridional vorticity gradient). However, increasing the q-flux anomaly further to $-125\,\mathrm{W/m^{-2}}$ leads to highly amplified anomalies with surface temperatures below 0°C at the Equator, indicating the potential for strong nonlinear feedbacks (although under somewhat unrealistically strong oceanic drivers).

It should be mentioned that there is considerable year-to-year variation in the QSW amplitude response, but the mean response appears to be a robust signal. This is because of the strong similarities of the results about the QSW patterns in the APEs and reanalysis and since this QSW pattern could be observed for all APEs and all seasons. This suggests that, during La Niña conditions, there is an increased likelihood of increased QSW amplitudes in the regions mentioned above. We further repeated the calculations of the QSWs with a fixed wavenumber range 4–11 and this confirms that the findings are not due to a strong sensitivity on the chosen, meridionally dependent, wavenumber range. Further support for the robustness of the findings of the QSW patterns can be given by the similar behaviour of the anomalous power spectra of the anomalous meridional wind in wavenumber–latitude phase space.

This paper therefore demonstrates that ENSO variability does impact on QSW activity, both locally in the Pacific, and more broadly across the Northern Hemisphere. As indicated by previous work (Wolf *et al.*, 2018b, 2020), such a relationship has potential impacts in terms of the likelihood of extreme weather associated with blocking in both North America and the Atlantic region. An interesting area for further research is therefore the potential implications for seasonal forecasting (i.e., potential links between La Niña and the potential increased likelihood of QSW affecting northern and western European weather at the weeks-to-months ahead range).

ACKNOWLEDGMENTS

The data for the 12-hourly envelope fields of the quasi-stationary waves for ERA-Interim, between 01 June 1979 and 31 August 2015, are available at the UK Centre for Environmental Data Analysis (Wolf *et al.*, 2018a) (without smoothing in the meridional direction, as described in Wolf *et al.* (2018b) and used here). We acknowledge funding from the Natural Environment Research Council (NERC) for the ODYSEA project (grant number: NE/M006085/1). NPK was funded by a NERC Independent Research Fellowship (NE/L010976/1). We would like to thank Arnaud Czaja for his input and fruitful discussions which helped to improve the presentation of our results.

AUTHOR CONTRIBUTIONS

G. Wolf: investigation; methodology; software; visualization; writing – original draft. **D.J. Brayshaw:** investigation; methodology; supervision; writing – review and editing. **N.P. Klingaman:** investigation; methodology; supervision; writing – review and editing.

ORCID

G. Wolf https://orcid.org/0000-0001-5704-6550

REFERENCES

Blackburn, M. and Hoskins, B.J. (2013) Context and aims of the aqua-planet experiment. *Journal of the Meteorological Society of Japan, Series II*, 91A, 1–15. https://doi.org/10.2151/jmsj.2013-A01.

Branstator, G. (2002) Circumglobal teleconnections, the jet stream waveguide, and the North Atlantic Oscillation. *Journal of Climate*, 15(14), 1893–1910. https://doi.org/10.1175/1520-0442(2002)015<1893:CTTJSW>2.0.CO;2.

Brayshaw, D.J., Hoskins, B.J. and Blackburn, M. (2008) The storm-track response to idealized sst perturbations in an aqua-planet gcm. *Journal of the Atmospheric Sciences*, 65(9), 2842–2860. https://doi.org/10.1175/2008JAS2657.1.

Brayshaw, D.J., Woollings, T. and Vellinga, M. (2009) Tropical and extratropical responses of the North Atlantic atmospheric circulation to a sustained weakening of the MOC. *Journal of Climate*, 22(11), 3146–3155. https://doi.org/10.1175/2008JCLI2594.1.

Chen, T.-C. (2002) A North Pacific short-wave train during the extreme phases of ENSO. *Journal of Climate*, 15(17), 2359–2376. https://doi.org/10.1175/1520-0442(2002)015<2359:ANPSWT>2.0.CO;2.

Dee, D.P., Uppala, S.M., Simmons, A.J., Berrisford, P., Poli, P., Kobayashi, S., Andrae, U., Balmaseda, M.A., Balsamo, G., Bauer, P., Bechtold, P., Beljaars, A.C.M., van de Berg, L., Bidlot, J., Bormann, N., Delsol, C., Dragani, R., Fuentes, M., Geer, A.J., Haimberger, L., Healy, S.B., Hersbach, H., Hólm, E.V., Isaksen, L., Kållberg, P., Köhler, M., Matricardi, M., McNally, A.P., Monge-Sanz, B.M., Morcrette, J.-J., Park, B.K., Peubey, C., de Rosnay, P., Tavolato, C., Thépaut, J.-N. and Vitart, F. (2011) The ERA-Interim reanalysis: configuration and performance of the data assimilation system. *Quarterly Journal of the Royal Meteorological Society*, 137, 553–597. https://doi.org/10.1002/qj.828.

Ding, Q.H. and Wang, B. (2005) Circumglobal teleconnection in the Northern Hemisphere summer. *Journal of Climate*, 18(17), 3483–3505. https://doi.org/10.1175/JCLI3473.1.

Fasullo, J.T. and Trenberth, K.E. (2008) The annual cycle of the energy budget. Part II: meridional structures and poleward transports. *Journal of Climate*, 21(10), 2313–2325. https://doi.org/10.1175/2007JCLI1936.1.

Gastineau, G., Li, L. and Le Treut, H. (2011) Some atmospheric processes governing the large-scale tropical circulation in idealized aquaplanet simulations. *Journal of the Atmospheric Sciences*, 68(3), 553–575. https://doi.org/10.1175/2010JAS3439.1.

Hirons, L.C., Klingaman, N.P. and Woolnough, S.J. (2015) MetUM-GOML: a near-globally coupled atmosphere–ocean-mixed-layer model. *Geoscientific Model Development*, 8, 363–379. https://doi.org/10.5194/gmd-8-363-2015.

Hoskins, B.J. and Ambrizzi, T. (1993) Rossby wave propagation on a realistic longitudinally varying flow. *Journal of the Atmospheric Sciences*, 50(12), 1661–1671. https://doi.org/10.1175/1520-0469(1993)050<1661:RWPOAR>2.0.CO;2.

Large, W., McWilliams, J. and Doney, S. (1994) Oceanic vertical mixing: a review and a model with a nonlocal boundary-layer parameterization. *Reviews of Geophysics*, 32, 363–403. https://doi.org/10.1029/94RG01872.

Manola, I., Selten, F., Vries, H. and Hazeleger, W. (2013) "Waveguidability" of idealized jets. *Journal of Geophysical Research: Atmospheres*, 118(18), 10432–10440. https://doi.org/10.1002/jgrd.50758.

Masato, G., Woollings, T. and Hoskins, B.J. (2014) Structure and impact of atmospheric blocking over the Euro-Atlantic region in present-day and future simulations. *Geophysical Research Letters*, 41(3), 1051–1058. https://doi.org/10.1002/2013GL058570. ISSN 1944-8007.

Merlis, T.M. and Held, I.M. (2019) Aquaplanet simulations of tropical cyclones. *Current Climate Change Reports*, 5(3), 185–195. https://doi.org/10.1007/s40641-019-00133-y.

Nakamura, H., Nakamura, M. and Anderson, J.L. (1997) The role of high- and low-frequency dynamics in blocking formation. *Monthly Weather Review*, 125(9), 2074–2093. https://doi.org/10.1175/1520-0493(1997)125<2074:TROHAL>2.0.CO;2.

Peatman, S.C. and Klingaman, N.P. (2018) The Indian summer monsoon in MetUM-GOML2: effects of coupling and resolution. *Geoscientific Model Development*, 11, 4693–4709. https://doi.org/10.5194/gmd-11-4693-2018.

Petoukhov, V., Rahmstorf, S., Petri, S. and Schellnhuber, H.J. (2013) Quasi-resonant amplification of planetary waves and recent Northern Hemisphere weather extremes. *Proceedings of the National Academy of Sciences of the USA*, 110(14), 5336–5341. https://doi.org/10.1073/pnas.1222000110.

Rose, B.E.J. and Ferreira, D. (2013) Ocean heat transport and water vapor greenhouse in a warm equable climate: a new look at the low gradient paradox. *Journal of Climate*, 26(6), 2117–2136. https://doi.org/10.1175/JCLI-D-11-00547.1.

Saulière, J., Brayshaw, D.J., Hoskins, B.J. and Blackburn, M. (2012) Further investigation of the impact of idealized continents and SST distributions on the Northern Hemisphere storm tracks. *Journal of the Atmospheric Sciences*, 69(3), 840–856. https://doi.org/10.1175/JAS-D-11-0113.1.

Screen, J.A. and Simmonds, I. (2014) Amplified mid-latitude planetary waves favour particular regional weather extremes. *Nature Climate Change*, 4(8), 704–709. https://doi.org/10.1038/nclimate2271.

Shabbar, A., Bonsal, B. and Khandekar, M. (1997) Canadian precipitation patterns associated with the Southern Oscillation. *Journal of Climate*, 10(12), 3016–3027. https://doi.org/10.1175/1520-0442(1997)010<3016:CPPAWT>2.0.CO;2.

Voigt, A., Biasutti, M., Scheff, J., Bader, J., Bordoni, S., Codron, F., Dixon, R.D., Jonas, J., Kang, S.M., Klingaman, N.P., Leung, R., Lu, J., Mapes, B., Maroon, E.A., McDermid, S., Park, J.Y., Roehrig, R., Rose, B.E.J., Russell, G.L., Seo, J., Toniazzo, T., Wei, H.H., Yoshimori, M. and Vargas Zeppetello, L.R. (2016) The tropical rain belts with an annual cycle and a continent model intercomparison project: TRACMIP. *Journal of Advances in Modeling Earth Systems*, 8(4), 1868–1891. https://doi.org/10.1002/2016MS000748.

Walters, D.N., Boutle, I.A., Brooks, M., Melvin, T., Stratton, R.A., Vosper, S., Wells, H., Williams, K.D., Wood, N., Allen, T., Bushell, A.C., Copsey, D., Earnshaw, P.D., Edwards, J.M., Gross, M., Hardiman, S., Harris, C.M., Heming, J., Klingaman, N.P., Levine, R.C., Manners, J.C., Martin, G., Milton, S.F., Mittermaier, M.M., Morcrette, C.J., Riddick, T., Roberts, M.J., Sanchez, C., Selwood, P., Stirling, A., Smith, C., Suri, D., Tennant, W., Vidale, P.L., Wilkinson, J.M., Willett, M.R., Woolnough, S.J. and Xavier, P.K. (2017) The Met Office Unified Model global atmosphere 6.0/6.1 and JULES global land 6.0/6.1 configurations. *Geoscientific Model Development*, 10(4), 1487–1520. https://doi.org/10.5194/gmd-7-361-2014.

Wolf, G., Brayshaw, D.J., Klingaman, N.P. and Czaja, A. (2018a) Envelope field of Northern Hemispheric upper tropospheric (300 hPa) quasi-stationary waves (June 1979 to August 2015). *Centre for Environmental Data Analysis archive*. https://doi.org/10.5285/c0c7998800414e46b6823dc75751bb4c.

Wolf, G., Brayshaw, D.J., Klingaman, N.P. and Czaja, A. (2018b) Quasi-stationary waves and their impact on European weather and extreme events. *Quarterly Journal of the Royal Meteorological Society*, 144, 2431–2448. https://doi.org/10.1002/qj.3310.

Wolf, G., Czaja, A., Brayshaw, D.J. and Klingaman, N.P. (2020) Connection between sea surface anomalies and atmospheric quasi-stationary waves. *Journal of Climate*, 33(1), 201–212. https://doi.org/10.1175/JCLI-D-18-0751.1.

Yeh, S.-W., Cai, W., Min, S.-K., McPhaden, M.J., Dommenget, D., Dewitte, B., Collins, M., Ashok, K., An, S.-I., Yim, B.-Y. and Kug, J.-S. (2018) ENSO atmospheric teleconnections and their response to greenhouse gas forcing. *Reviews of Geophysics*, 56(1), 185–206. https://doi.org/10.1002/2017RG000568.

Yen, M.-C. and Chen, T.-C. (2002) A revisit of the tropical-midlatitude interaction in east Asia caused by cold surges. *Journal of the Meteorological Society of Japan. Ser. II*, 80(5), 1115–1128. https://doi.org/10.2151/jmsj.80.1115.

Zhang, L., Zhi, X. and Yang, H. (2011). The relationship between the cold surge over the NSCS amp; the ENSO events, *International Conference on Information Science and Technology*, pp. 126–131, DOI 10.1109/ICIST.2011.5765225, (to appear in print).

Zimin, A.V., Istvan Szunyogh, D.J., Patil, B.R. and Edward, O. (2003) Extracting envelopes of Rossby wave packets. *Monthly Weather Review*, 131(5), 1011–1017. https://doi.org/10.1175/1520-0493(2003)131<1011:EEORWP>2.0.CO;2.

How to cite this article: Wolf, G., Brayshaw, D. & Klingaman, N. (2022) Response of atmospheric quasi-stationary waves to La Niña conditions in Northern Hemisphere winter. *Quarterly Journal of the Royal Meteorological Society*, 1–12. Available from: https://doi.org/10.1002/qj.4261